Ocean Dynamics (2012) 62:105–121
DOI 10.1007/s10236-011-0465-9

Wind-speed inversion from HF radar first-order backscatter signal

Wei Shen · Klaus-Werner Gurgel · George Voulgaris · Thomas Schlick · Detlef Stammer

Received: 2 February 2011 / Accepted: 20 June 2011 / Published online: 11 August 2011

Abstract Land-based high-frequency (HF) radars have the unique capability of continuously monitoring ocean surface environments at ranges up to 200 km off the coast. They provide reliable data on ocean surface currents and under slightly stricter conditions can also give information on ocean waves. Although extraction of wind direction is possible, estimation of wind speed poses a challenge. Existing methods estimate wind speed indirectly from the radar derived ocean wave spectrum, which is estimated from the second-order sidebands of the radar Doppler spectrum. The latter is extracted at shorter ranges compared with the first-order signal, thus limiting the method to short distances. Given this limitation, we explore the possibility of deriving wind speed from radar first-order backscatter signal. Two new methods are developed and presented that explore the relationship between wind speed and wave generation at the Bragg frequency matching that of the radar. One of the methods utilizes the absolute energy level of the radar first-order peaks while the second method uses the directional spreading of the wind generated waves at the Bragg frequency. For both methods, artificial neural network analysis is performed to derive the interdependence of the relevant parameters with wind speed. The first method is suitable for application only at single locations where in situ data are available and the network has been trained for while the second method can also be used outside of the training location on any point within the radar coverage area. Both methods require two or more radar sites and information on the radio beam direction. The methods are verified with data collected in Fedje, Norway, and the Ligurian Sea, Italy using beam forming HF WEllen RAdar (WERA) systems operated at 27.68 and 12.5 MHz, respectively. The results show that application of either method requires wind speeds above a minimum value (lower limit). This limit is radar frequency dependent and is 2.5 and 4.0 m/s for 27.68 and 12.5 MHz, respectively. In addition, an upper limit is identified which is caused by wave energy saturation at the Bragg wave frequency. Estimation of this limit took place through an evaluation of a year long database of ocean spectra generated by a numerical model (third generation WAM). It was found to be at 9.0 and 11.0 m/s for 27.68 and 12.5 MHz, respectively. Above this saturation limit, conventional second-order methods have to be applied, which at this range of wind speed no longer suffer from low signal-to-noise ratios. For use in operational systems, a hybrid of first- and second-order methods is recommended.

Responsible Editor: Michel Rixen

This article is part of the Topical Collection on *Maritime Rapid Environmental Assessment.*

W. Shen · K.-W. Gurgel (✉) · T. Schlick · D. Stammer
Institute of Oceanography, University of Hamburg,
Bundesstrasse 53, 20146, Hamburg, Germany
e-mail: gurgel@ifm.uni-hamburg.de

W. Shen
e-mail: wei.shen@zmaw.de

T. Schlick
e-mail: thomas.schlick@zmaw.de

D. Stammer
e-mail: detlef.stammer@zmaw.de

G. Voulgaris
Department of Earth and Ocean Sciences,
University of South Carolina,
Columbia, SC 29208, USA
e-mail: gvoulgaris@geol.sc.edu

Keywords Coastal wind speed · HF radar · Neural network · Wave generation

1 Introduction

Wind energy provides the majority of forcing on the surface of the ocean and as such plays an important role in driving a variety of oceanographic phenomena including water circulation and wave generation with implications that extend from local and regional (e.g., upwelling) to global (e.g., air–sea gas exchanges) scales. Wind measurements at sea present one of the first environmental observations carried out by seamen even before the advance of technology. It is characteristic that the first observations were carried out visually using sea state as a proxy (see Beafourt scale), a principle utilized by the remote sensing techniques available over the last few decades. Microwave radars (e.g., scatterometers), give a strong backscatter signal from the short ripple waves (3–5 cm), which react very fast to changes in the wind field. This signal is then used to provide reliable wind measurements from the ocean surface. Such technologies as those used in spaceborne scatterometry (cf. Schroeder et al. 1985) and Synthetic Aperture Radar (SAR) (cf. Monaldo et al. 2001; Fisher et al. 2008) provide wind information over large areas but with a temporal resolution that is limited by their orbit repetition time that may extend to several days.

Stationary, shore-based high-frequency (HF) radars provide an alternative method for covering large areas, up to 200 km off the coast and with high temporal resolution ($\leq$ 1 h). HF radars can deliver real-time data at relatively high spatial resolutions (300–1500 m) and can be installed, operated, and maintained in all weather conditions at a reduced cost compared with satellite or in situ sensor technology. HF radars are used routinely to measure ocean surface currents (e.g., Barrick 1977b; Wyatt et al. 2006; Parks et al. 2009) , ocean wave spectra (e.g., Barrick 1977a, c; Wyatt 1986; Gurgel et al. 2006; Haus et al. 2010), and even wind direction (e.g., Heron and Rose 1986; Harlan and Georges 1994; Wyatt et al. 2006). However, the measurement of wind speed still poses a challenge. HF radars couple to much longer (5–12 m) Bragg resonant ocean waves than microwaves and, thus, need longer time to respond to changing wind conditions. Most existing methods (cf. Dexter and Theodorides 1982; Green et al. 2009) utilize the whole or part of the wave spectrum obtained from analysis of the second-order signal (see Section 2) to extract wind speed information and they assume that the ocean wave spectrum is in equilibrium with the prevailing wind. However, the use of the second-order signal suffers from reduced range coverage (when compared with the first-order signal) and also there might be parts of the ocean spectrum contributing to the second-order signal that are not related to local wind conditions (e.g., swell). Stewart and Barnum (1975) suggested wind speed derivation from the widening of the first-order Bragg peaks, but their approach using sky-wave HF radar data was found to be limited (cf. Green et al. 2009). With these limitations in mind, we investigate the potential of using Bragg resonant ocean waves for wind speed retrieval as this is a stronger signal compared with the second-order signal. Vesecky et al. (2005) have also presented a method for the estimation of wind information from first-order signals. However, their method exploits the near-surface current shear that can be estimated using multi-frequency systems. Application of the method with single-frequency systems, as in this study, requires further research, something beyond the scope of this paper.

The objective of this work is to develop a new method to estimate wind speed based on the first-order Bragg peaks from single-frequency systems. Given the non-linearity of the problem, artificial neural networks (ANNs) are used to establish the complex relationship between wind speed and first-order radar signal. Our hypothesis is that if an ANN is trained with a sufficiently variable set of in situ data, covering a wide range of conditions, then it can be used to estimate the local wind speed from the first-order Bragg peaks.

This paper is organized in sections dealing with specific issues. Section 2 provides a brief description of the operation of the HF radars, the signal they record, and its relation to wind-generated ocean waves. In Section 3, the relations between wind speed, Bragg frequency, and directional spreading, with respect to radar signals are explored and new wind inversion methods are developed. The experimental setups and data used to test our methods are presented in Section 4. The results from applying the new methods to the experimental data are shown in Section 5 together with a discussion on our findings. Finally, the conclusions are presented in Section 6.

2 Background

The HF radio band covers frequencies 3–30 MHz which correspond to wavelengths 100–10 m. The radar transmitted electromagnetic (EM) wave is coupled with the ocean surface at the air–sea interface and propagates beyond the horizon following the curvature of the earth. Some energy of the sea-surface-coupled EM wave is scattered back to the radar by the surface ocean waves.

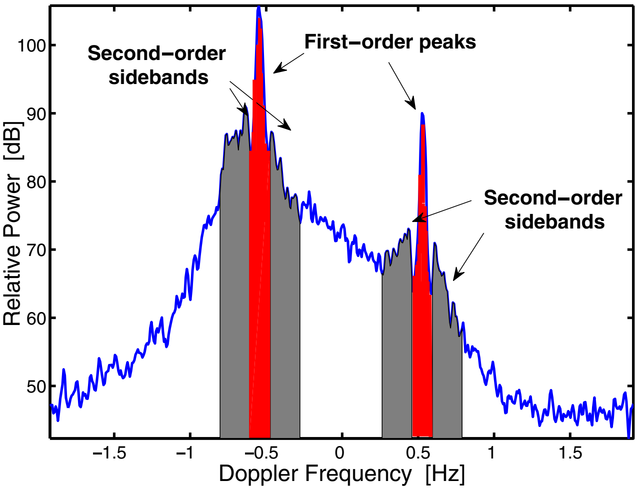

Fig. 1 An example of a measured Doppler spectrum at 27.65 MHz radar frequency showing the location of the first-order Bragg peaks and the second-order sidebands marked in *gray*, where the strongest signals within the continuum generated by second-order interaction can be expected

The strongest signal observed by the radar receiver is due to scattering from ocean waves with a wavelength λ_w which is half the wavelength of the emitted EM wave λ_el (cf. Crombie 1955). This process is known as Bragg scattering and leads to a pair of distinct peaks located on either side of the 0 Hz line. In case of still water, i.e., without any ocean current, these first-order Bragg peaks appear at a Doppler frequency of $f_\mathrm{B} = \pm 2c_\mathrm{p}/\lambda_\mathrm{el}$ caused by the phase velocity $c_\mathrm{p} = \sqrt{g\lambda_\mathrm{w}/2\pi}$ of the Bragg resonant ocean waves moving toward and away from the radar, where g is acceleration due to gravity. An example of a radar Doppler spectrum and the associated Bragg signal is shown in Fig. 1.

The energy found around the two first-order Bragg peaks is due to second-order interaction between the transmitted EM wave and two ocean waves which generates a continuum around the first-order Bragg peaks. The strongest contributions within the continuum are usually referred to as "second-order sidebands" and shown in Fig. 1. Hasselmann (1971) was first to suggest that the "second-order interactions yield a two sided image of the surface wave spectrum on either side of the first-order Bragg line." This relationship was quantified initially by Barrick (1972b) and later on by Gill and Walsh (2001), who introduced the equations for the first- and second-order cross-sections describing the EM/ocean wave scattering process.

2.1 Range dependency

The propagation of the radar emitted EM wave depends on the transmitted power P_{tr}, but it is also subject to attenuation that reduces the effective range of the system. Attenuation depends on a number of parameters including sea conductivity (i.e., salinity and temperature), radar frequency (cf. Gurgel et al. 1999b), thermal and atmospheric noise (cf. Shearman 1983), and radio interference. In addition, sea state influences propagation of the EM wave (cf. Barrick 1971a, b; Forget et al. 1982). Range increases with increasing sea state due to a stronger backscatter signal but at the same time attenuation increases due to loss of power by stronger backscatter at shorter ranges. Overall, the total loss of power with range is usually described by a "path loss" parameter denoted as A_r.

Figure 2 shows a range-dependent Doppler spectrum obtained with a 12.5-MHz Wellen radar (WERA) radar system. It is noticeable that the first-order peaks extend as far as 120 km in range while the second-order sidebands contain less energy than the first-order peaks and, thus, cannot be traced at ranges exceeding 40 km. This example was obtained under low sea state conditions (significant wave height $\mathrm{H_s} = 0.7\,\mathrm{m}$). Under higher wave conditions the power of the second-order sidebands increases leading to extended ranges (i.e., approximately 60 km at $\mathrm{H_s} = 1.5\,\mathrm{m}$, not shown here). As a consequence, utilization of first-order peaks could lead to extraction of environmental parameters over longer range than the use of the second-order signal.

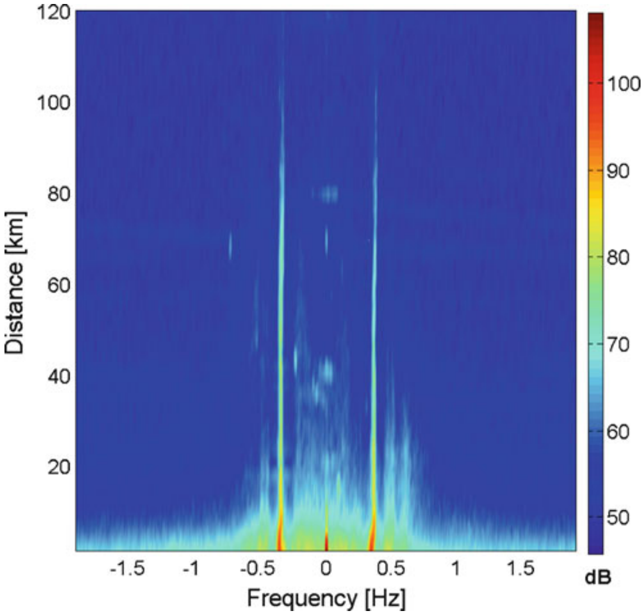

Fig. 2 An example of a measured RD spectrum at 12.5 MHz radar frequency showing the strong first-order Bragg peaks and the associated second-order sidebands as a function of range. This spectrum was acquired during the Ligurian Sea experiment at Palmaria, 05/30/2009, 03:06 UTC with a coherent integration time of 18 min

This is particular true for low sea state conditions and low radar frequencies (cf. Barrick 1977a).

2.2 Wind speed and direction estimation from HF radars

For over 30 years, first-order Bragg peaks have been used to estimate the velocity component (radial) of the ocean surface along the direction of the HF radar beam (cf. Barrick 1977b). This application is now well accepted worldwide and HF radars increasingly become an integral component of ocean monitoring systems (cf. Gurgel et al. 2011; Savidge et al. 2011). On the other hand, second-order sidebands can be used to derive non directional ocean wave spectra (cf. Barrick et al. 1974) or wave height (cf. Heron and Prytz 2002). Gurgel et al. (2006) provided an empirical method to estimate the ocean wave spectrum from the second-order sidebands, that is extended to the directional spectrum when information from two stations are available. Also Wyatt (1986) and Wyatt et al. (2006) have presented a method to invert Barrick et al.'s (1974) integral equation for the second-order cross section; it uses the measured second-order Doppler spectrum to estimate the ocean directional wave spectrum. More recently, Haus et al. (2010) suggested a method to correct the bias in ocean wave height estimates from a single radar site introduced by the angle between the radio beam and wave direction.

Wind direction can be derived from evaluating the ratio of the two first-order Bragg peaks from at least two radar sites. If the radar frequency is high (25–30 MHz), the Bragg resonant waves are relatively short (6–5 m) and they closely follow changes in the wind field.

Except for an early approach by Stewart and Barnum (1975) and the multi-frequency method by Vesecky et al. (2005), wind speed derivation techniques to date are based on the analysis of the second-order sidebands. Dexter and Theodorides (1982) provided a method using wave height ($\mathrm{H_s}$) and peak frequency ($\mathrm{f_p}$) to estimate wind speed by relating these parameters to wind speeds required to generate waves with similar characteristics. Likewise, if we assume that the ocean waves are in equilibrium with the wind field, a Pierson–Moskowitz type ocean wave spectrum (cf. Pierson and Moskowitz 1964) can be formulated. Green et al. (2009) used this estimated wave spectrum as a forcing to simulate the second-order sidebands within the radar Doppler spectrum with the model described by Gill and Walsh (2001); a relationship was established that relates the peak frequency of the simulated second-order sideband to $\mathrm{f_p}$ of the wind-driven ocean wave spectrum. This relationship was then used to extract wind speed from the observed peak in the radar second-order sidebands. This method, although promising, was verified with a limited data set of only 7.5 h covering a very narrow range of wind conditions.

Overall, the use of second-order sidebands for wind inversion suffers from the fact that these signals contain information on the ocean wave spectrum, which might not always represent only local wind conditions. The use of a Pierson-Moskowitz or JONSWAP spectrum (cf. Hasselmann et al. 1980) as a transfer function between second-order radar signal and wind speed is valid only if the wind speed is high enough to dominate the ocean wave spectrum (i.e., $U_{10} \geq c_p$, where c_p is the spectral peak-wave phase speed). If the wind speed decreases, the spectrum is no longer in equilibrium with the prevailing wind conditions. Also, if swell waves are present and the full wave spectrum is not available to distinguish frequency ranges corresponding to wind conditions, then the assumed Pierson–Moskowitz or JONSWAP spectra will have a peak frequency which is shifted toward lower frequencies than the spectra corresponding to pure wind-generated waves. In this case, the assumed transfer relationship between driving wind speed and ocean waves can lead to incorrect results.

3 Methods

In this section, the relationships between wind speed and direction to ocean waves at specific frequencies corresponding to a radar's Bragg resonant frequency are developed. This is carried out in order to identify any limits imposed in relating wind-speed estimates to first-order radar Doppler spectral peaks.

3.1 Wind speed and Bragg frequency

As explained earlier, radars can only provide signals that reflect ocean wave conditions. Any attempt to obtain wind information assumes utilization of the relationship between wind forcing and wave generation. The use of the first-order peak of the radar Doppler spectrum restricts the applicability of this transfer function to a single frequency of the ocean wave spectrum that corresponds to the radar frequency dependent Bragg resonant ocean waves. There is also a dependency on the radar look direction which is discussed in the context of first-order Bragg scattering and directional spreading in Section 3.3.

The restriction in frequency poses some limitations on the ranges of wind speeds that the particular Bragg frequency responds to. These limitations could be defined using a theoretical ocean spectrum in equilibrium with the prevailing wind conditions (e.g., JONSWAP or Pierson–Moskowitz). However, these spectra assume stationary equilibrium conditions with the wind. An alternative method is to use ocean wave spectra that have been estimated numerically under non stationary conditions.

With this in mind, ocean spectra generated in the frame of HIPOCAS (cf. Soares 2008), have been investigated. HIPOCAS is an EU-funded project designed to obtain a 40-year hindcast of wind, wave, sea level, and ocean current climatology for European waters and coastal seas. High-resolution wave spectral data were generated using a third generation version of WAM (cf. Hasselmann et al. 1988) run in a nested grid approach. WAM is a non-stationary surface wave prediction model based on the energy density balance equation in both frequency and direction coordinates.

One year of three-hourly data of wind speed and direction as well as ocean wave directional spectra from seven locations within the North Sea were available. The hindcasted wave directional spectra used, consisted of 28 frequency bins covering the range 0.04–0.55 Hz and with a directional resolution of 15°. An example of the WAM-generated directional spectra is shown in Fig. 3 where three wave components can be identified. The wave system with the highest energy travels toward the southeast and has a frequency of approximately 0.1 Hz. These waves are identified as swell and, thus, they are not related to local wind forcing. The wave component in the frequency band 0.2–0.4 Hz traveling toward the northeast is aligned with the local wind direction. These waves represent the wind sea component of the wave spectrum which is suitable for wind inversion. The third wave component traveling toward the southsouthwest is a weak wind sea component remaining from previous wind forcing. Another important aspect relevant to this work is the behavior of the directional spreading. The directional spreading of the swell is much narrower than that of the wind seas and this is something that can be exploited further for identifying wind generated waves.

In order to investigate how the waves at a certain frequency react to different wind speeds, 1 year of WAM-generated spectra were analyzed. Spectra from a single location (3.00° E, 55.10° N) in the middle of the North Sea, over 200 km away from the coast were selected. Each individual frequency band from each energy spectrum was integrated over all directions, and the total energy corresponding to frequency bands of 0.28, 0.34, and 0.55 Hz were selected. These frequency values correspond to the frequency of Bragg resonant waves f_B that could be seen by HF radars operating at 7.59, 11.11, and 28.81 MHz, respectively. A scatter plot of each frequency specific wave energy *vs.* the corresponding wind speed conditions is shown in Fig. 4. The scatter plot shows that the wave energy increases with wind speed, with the rate of increase being higher at lower frequencies. In addition, at least for the two highest frequency bands (0.34 and 0.55 Hz) there is a clear upper limit in wind speed. Beyond that limit the wave energy at that frequency band seizes increasing and reaches a saturation point. Saturation levels can be observed at approximately 9 and 11 m/s for the 28.81 and 11.1 MHz radar frequency bands. Even for the lowest frequency band of 7.59 MHz a threshold of 15 m/s can be identified. These thresholds denote the upper wind speeds that can potentially be detected with the radar systems.

In addition, some lower limits can be identified in the figure. Theoretical arguments (cf. Hasselmann et al.

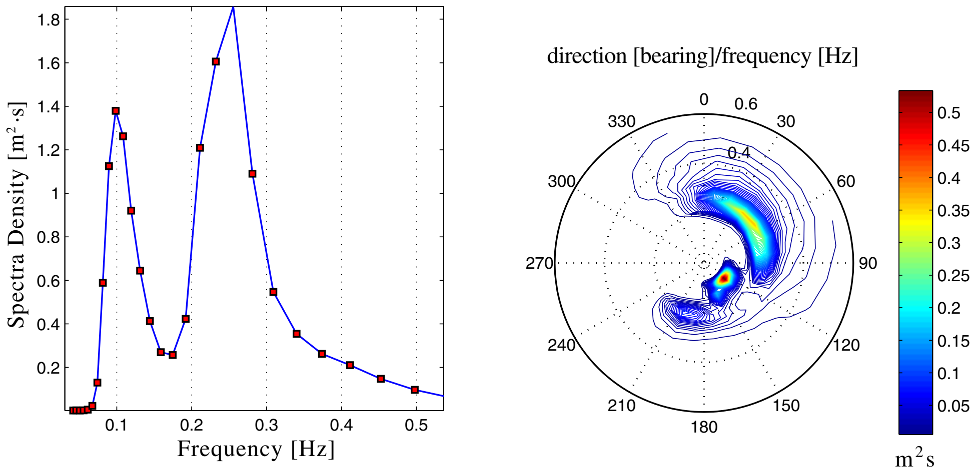

Fig. 3 Example of an ocean wave directional spectrum (*right panel*) and its associated non-directional wave spectrum (*left panel*) estimated by WAM used in HIPOCAS at 05/03/2004 09:00 UTC, 54.7°N 5.0°E (40 m water depth). Direction is "going to"

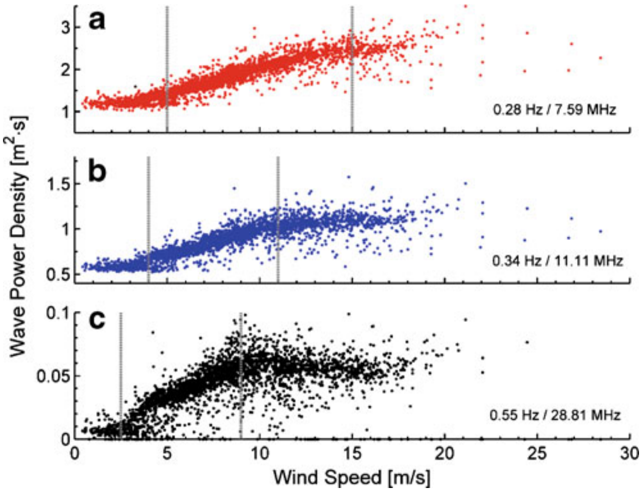

Fig. 4 Wave energy density levels at specific frequencies corresponding to Bragg waves for radars operated at **a** 7.59 MHz, **b** 11.11 MHz, and **c** 28.81 MHz plotted against local wind speed. *Vertical lines* show upper and lower limits of regions where the rate of increase of wave energy is proportional to wind speed. The lower limit is derived theoretically (see text), while the upper limit delineates the wind speed where energy starts saturating. Wave energy levels were estimated using WAM derived wave spectra from the North Sea

1980) suggest that for the selected frequencies the wind speed should be larger than the phase speed of the particular Bragg ocean waves. Assuming deep water conditions, wind speeds of 5, 4, and 2.5 m/s are estimated as lower limits for radar frequencies of 7.59, 11.11, and 28.81 MHz, respectively. These wind speeds appear to be close to those identified in Fig. 4 as the locations of changing slope in the wave power *vs.* wind speed diagram.

The relationship between wave power density and local wind speed for a given wave frequency band (Fig. 4) suggests that the wind speed can be inverted from wave power density until a frequency dependent upper threshold is reached. Beyond that threshold, however, wave power density reaches a saturation level where it remains relatively constant despite an increase in wind speed. Note that WAM is estimating the processes at the ocean surface and does not incorporate EM scattering processes which, especially at high HF frequencies (28 MHz), will result in an additional decrease of first-order backscatter power with increasing wind speed (cf. Barrick 1971a, b; Forget et al. 1982).

3.2 Wind speed and wave directional spreading

In addition to the dependency of the wave energy on wind speed described above, the directional spreading of the wave directional distribution varies with wind speed. Although a number of directional distributions have been identified (e.g., Apel 1994; Donelan and Pierson 1987; Elfouhaily et al. 1997; Kudryavtsev et al. 2005) in here we focus our discussion on the hyperbolic secant function presented by Donelan et al. (1985), as this is identified to give the most realistic up/down wind ratio conditions for 5 to 20 m long ocean waves (cf. Gurgel et al. 2006):

$$G(\theta) = 0.5\beta \cdot \mathrm{sech}^2(\beta \cdot \theta) \tag{1}$$

where β is the directional spreading parameter which has been shown to be a function of the ratio f/f_p, and θ is an angle referenced to the mean wave direction. Banner (1990), Banner et al. (1989) using data from a high-resolution pitch and roll buoy showed that the directional spreading parameter can be expressed as:

$$\beta = \begin{cases} 2.28(f/f_\mathrm{p})^{-0.65} & ; 0.97 < f/f_\mathrm{p} \le 2.56 \\ 10^{-0.4+0.8393\exp[-0.567\ln(f/f_\mathrm{p})]} & ; f/f_\mathrm{p} > 2.56 \end{cases} \tag{2}$$

In HF radar applications and for the first-order peak applications discussed in here the frequency f of the ocean waves in Eq. 2 corresponds to that of the Bragg resonant waves f_B. The wave peak frequency f_p, on the other hand, is related to wind speed and assuming a JONSWAP wave spectrum (cf. Hasselman et al. 1973) it is given by:

$$f_\mathrm{p} = \frac{11.0}{\pi}\left[g^2/(U_{10}F)\right]^{1/3} \tag{3}$$

where F is the fetch of the wind and U_{10} is the wind speed measured at 10 m above the sea surface. Thus, Eq. 3 together with the radar frequency can be used to derive the ratio f/f_p which in here corresponds to $f_\mathrm{B}/f_\mathrm{p}$. The relationship shown in Eq. 3 indicates that at locations close to land (i.e., small fetch), the f_p value becomes very large. So care should be taken that the ratio $f_\mathrm{B}/f_\mathrm{p} > 1$. This is a radar frequency dependent limitation as lower frequency radars resonate with longer waves and as such are more susceptible to this limit. In addition, the wave age as described by the ratio U_{10}/c_p might affect the directional spreading of the waves (cf. Hasselmann et al. 1980; Donelan et al. 1985), especially for higher frequencies.

3.3 HF radar first-order backscatter

In the following, we consider the radar echoes from a given surface area (patch) A_patch of the ocean given in radial coordinates. The size of this area is defined by its range r from the radar site, range cell width Δr, and beam width $\Delta\phi$. The radar look direction is given by its azimuth ϕ_0. In addition, the range r controls signal attenuation (or path loss) defined earlier as A_r (see Section 2).

The directional distribution $G(\theta_\mathrm{B})$ of the Bragg resonant waves and the radio beam direction ϕ_0 determine the wave components receding and approaching the radar site which correspond to the first-order peaks at negative and positive Bragg frequencies, respectively. The wind direction is assumed to be identical to the direction of the short Bragg resonant waves (wind sea). In order to explore this directional dependence of the first-order Bragg peak, we first present the first-order cross-section as it was originally formulated by Barrick (1972a):

$$\sigma_1(\omega) = 2^6\pi k_0^4 \sum_{m=\pm1} S(-2m\mathbf{k}_0)\delta(\omega - m\omega_\mathrm{B}) \tag{4}$$

where $k_0 = 2\pi/\lambda_{EM}$ is the magnitude of the radar wavenumber vector $\mathbf{k}_0$, $S(\cdot)$ is the ocean wave spectrum, $\omega_\mathrm{B} = 2\pi f_\mathrm{B}$ is the angular Bragg frequency, and $\delta(\cdot)$ is the Dirac function. The power of the first-order Bragg peaks

$$P_1(\pm\omega_\mathrm{B}) = P_{tr}\cdot A_r\cdot A_\mathrm{patch}\cdot\sigma_1(\pm\omega_\mathrm{B}) \tag{5}$$

is calculated from the transmitted power P_{tr}, the range dependent signal attenuation A_r, the ocean's patch size A_patch and the cross-section σ_1.

As Eq. 5 indicates, this power is proportional to the energy of the Bragg resonant waves. The latter is inserted into Eq. 5 through the spectral energy $S(\cdot)$ (see Eq. 4). Combining Eqs. 4 and 5, the directional dependence of the power of the first-order peaks can be quantified using:

$$\begin{aligned} P_1(+f_\mathrm{B}) &= \kappa\cdot E(f_\mathrm{B})\cdot G(\pi+\phi_0-\theta_\mathrm{B}) \\ P_1(-f_\mathrm{B}) &= \kappa\cdot E(f_\mathrm{B})\cdot G(\phi_0-\theta_\mathrm{B}) \end{aligned} \tag{6}$$

where κ is a radar dependent, proportionality factor that can be derived from Eqs. 4 and 5. $E(f_\mathrm{B})$ is the ocean wave power $S(\cdot)$ at Bragg frequency integrated over all directions.

From Eq. 6, it is obvious that the power ratio of the radar first-order peaks is defined by the ratio of the directional spreading of the Bragg ocean waves so that:

$$R(f_\mathrm{B}) = \frac{P_1(+f_\mathrm{B})}{P_1(-f_\mathrm{B})} = \frac{G(\pi+\phi_0-\theta_\mathrm{B})}{G(\phi_0-\theta_\mathrm{B})} \tag{7}$$

In summary, wind speed and wave directional spreading are closely related to each other (see Section 3.2). In addition, wind speed affects the power of the first-order peaks by controlling the wave energy spectrum (see Eq. 6). Assembling all these dependencies, we can show that wind speed depends on a number of variables that can be measured using HF radar technology. This can be expressed as:

$$U_{10} = \mathcal{F}(P_1(+f_\mathrm{B}), P_1(-f_\mathrm{B}), G(\phi_0-\theta_\mathrm{B}), \phi_0) \tag{8}$$

where $\mathcal{F}(\cdot)$ is a non-linear transfer function knowledge of which would allow its use for wind-speed inversion. Required parameters in this function are the positive and negative first-order peak power $P_1(\pm f_\mathrm{B})$, the directional distribution of Bragg waves $G(\phi_0-\theta_\mathrm{B})$ and the radio beam direction ϕ_0. In case of a single radar site, only the two first-order peaks and the radio beam direction are available and no directional distribution can be resolved. If a second radar is available, which looks at the same area of the ocean but from a different angle, this ambiguity can be solved and $G(\phi_0-\theta_\mathrm{B})$ can be estimated using a mathematical function. This function could be a secant function with an assumed spreading value β. However, in reality $G(\phi_0-\theta_\mathrm{B})$ could be of a different shape and not always described analytically. We, therefore, propose the solution of this problem using appropriately trained ANNs.

3.4 Wind-speed inversion using a neural network

ANNs are often used in applications where, although a relationship is expected between two groups of parameters, the exact form of the relationship is either unknown or too complicated to be described analytically. In such cases, the ANN can be trained through a learning procedure that utilizes data from both groups (i.e., input and output). If the training exercise is successful then the "educated" ANN can be used with input data to provide the wanted output (target data). This concept is applied in here, where the transfer function shown in Eq. 8, is the one that the ANN is trying to simulate. In this application, the radar-derived quantities with strong dependence on wind speed (i.e., power of first-order peaks, directional spreading, etc.) are the input data to the ANN, while the in situ wind data are the target data. A two-layer feed-forward ANN utilizing error back-propagation (cf. Rumelhart et al. 1986) trained with a Levenberg–Marquardt algorithm (cf. Marquardt 1963) is applied using MatLab's® Neural Network Toolbox.

3.4.1 Wind-speed inversion using the power of first-order peaks

For cases where both the training data set (i.e., in situ wind speed and direction) and the input data sets (i.e., radar derived quantities) are from the same location, radar range (r) and radio beam direction (ϕ_0) are constant. In such cases, any significant variations in the power of the first-order signal are predominantly due to variations in the wind-induced ocean wave signal. Although small variabilities due to environmental conditions (e.g., atmospheric influences, variability of intertidal zone width in front of the radars, etc.) are possible, these are less significant and can be ignored.

In this case, the data being input to the ANN (Fig. 5, left side) are provided by the positive and negative first-order power peaks, $P_{1i}(+f_\mathrm{B})$ and $P_{1i}(-f_\mathrm{B})$, obtained by at least two radars at sites denoted by $i = 1, 2$. The dashed and black filled areas in Fig. 5 refer to the specific wave directions that cause the Bragg backscattering measured by the two radar sites. The target data (see Fig. 5, right side) are in situ wind speed and direction.

Although there are various methods available for the selection of data to be used in training a neural network (cf. Rojas 1996), in this work we elected to use the method called random data division (cf. Demuth et al. 2009). This method selects data randomly from our existing data set ensuring inclusion of all environmental conditions encountered during the field experiments. In the selection of the training, validation and testing data sets the common practice (cf. Kaastra and Boyd 1996) requires the training set to be the largest one while the testing set should vary between 10% and 30% of the total data set. For this work, we elected 60% as the training data set and we split the remaining data into validation (20%) and test (20%) data sets. The training data set is used to adjust the ANNs internal weights while the validation data set is used during the recursive training steps to find the point of best ANN prediction while avoiding over-fitting. Thus, while both training and validation data sets are used to formulate the ANN model, the test data set is used to independently test the final result. The ANN employed in this case uses four input neurons, twelve neurons in the hidden layer and three neurons in the output layer.

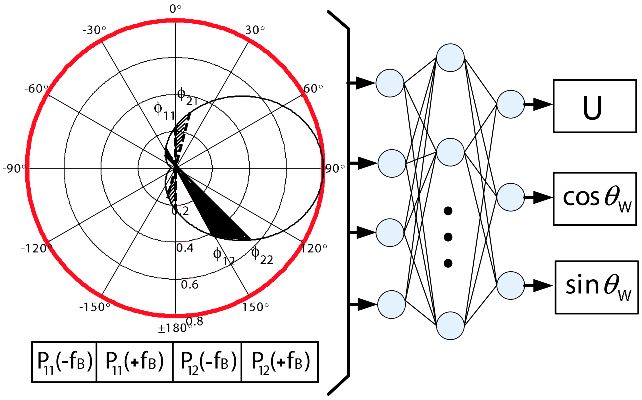

Fig. 5 Schematic diagram of the first-order peak power wind inversion technique. *Left*, ANN input data consisting of two pairs of first-order peak power. The radar look direction ϕ_0 is in the center of the beam given by its bounds ϕ_1 and ϕ_2. *Right*, ANN output data consisting of wind speed and direction

3.4.2 Wind-speed inversion using the directional distribution of Bragg waves

At locations within an area covered by two or more radars, that differ from that with in situ data availability, the radar ranges (r) and radio beam directions (ϕ_0) between the ANN training location and inversion locations are different. This results in variations of the power of the first-order signal due to path loss (A_r) and differences in the relative angle between radio beam and the Bragg ocean wave directional distribution, even if the wind conditions are identical at the two locations. As a result, an ANN trained with data at a particular location could be used at other locations only if a correction for range and direction differences is applied to the radar signal prior to inversion. Alternatively, other parameters should be used for wind inversion (i.e., both ANN training and prediction) that do not depend on radar range and direction.

In this case, utilization of the dependency of wind speed on directional spreading (β) as presented in Section 3.2 is exploited. The mean wave direction of the Bragg ocean wave can be estimated from the ratio of the first-order Bragg peak power by combining Eqs. 6 and 1 and solving for the mean wave direction:

$$\theta_\mathrm{B} = \phi_{0i} \pm \frac{1}{2\beta} \ln \left| \frac{1 - \sqrt{R_i} e^{(-\beta \cdot \pi)}}{\sqrt{R_i} e^{(\beta \cdot \pi)} - 1} \right| \quad \text{for} \quad i = 1, 2 \qquad (9)$$

where Ri is the ratio of the first-order radar signal power from station i (Eq. 7). Thus, solving this system of two equations, one for each radar site ($i = 1, 2$), a unique solution for the mean wave direction (θ_B) and the spreading parameter (β) can be obtained. These values are then used in the ANN training, with the wave direction (θ_B) converted into vector form consisting of sine and cosine components. These three quantities are taken for the specific radar beams and ranges pointing to the particular area of the ocean where in situ wind direction and speed data are available.

As shown schematically in Fig. 6, the ANN utilized in this case uses three input neurons, ten neurons in the hidden layer, and three neurons in the output layer. As

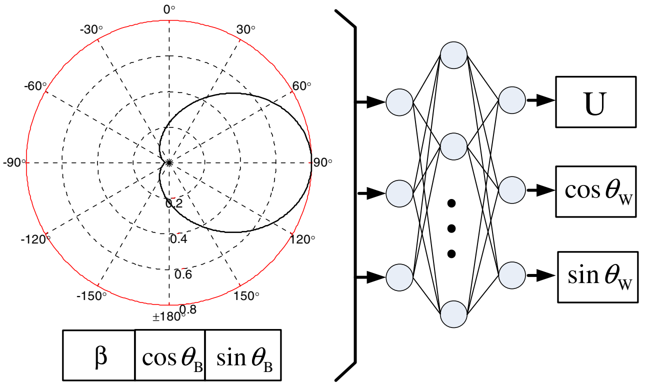

Fig. 6 Schematic diagram of the "directional distribution" wind inversion technique. *Left*, ANN input data consisting of spreading parameter (β) and wave direction (θ_B) at Bragg frequency. *Right*, ANN output data consisting of wind speed and direction (θ_W)

in the previous case, training, validation, and testing is carried out using 60%, 20%, and 20% of the wind data samples, respectively.

Once the ANN is trained, θ_B and β values can be calculated for other locations within the radar coverage area using Eq. 9. These values are then passed into the ANN which estimates wind speed and direction within the area covered by both radars. The advantage of this method compared with the ANN described in Section 3.4.1 is that it allows for "spatial extension" to the whole radar coverage area.

4 Data collection

Data sets from two HF radar deployments have been used to evaluate the inversion methods outlined in the previous section. Different experimental setups and radar frequencies were used in each experiment and the details are described below.

The first deployment occurred at the Ligurian Sea, Italy, and provided data for a period of 3 months from 7 May to 17 July 2009. During this experiment, the radars were installed on the island of Palmaria and in San Rossore close to Pisa (see Fig. 7, left). The second deployment was carried out as part of the "European Radar Ocean SEnsing" (EuroROSE) (cf. Günther et al. 1998) experiment conducted in Fedje, Norway, during the period 8 February to 3 April 2000. Two radars were installed on the islands of Fedje and Lyngøy, respectively (see Fig. 7, right).

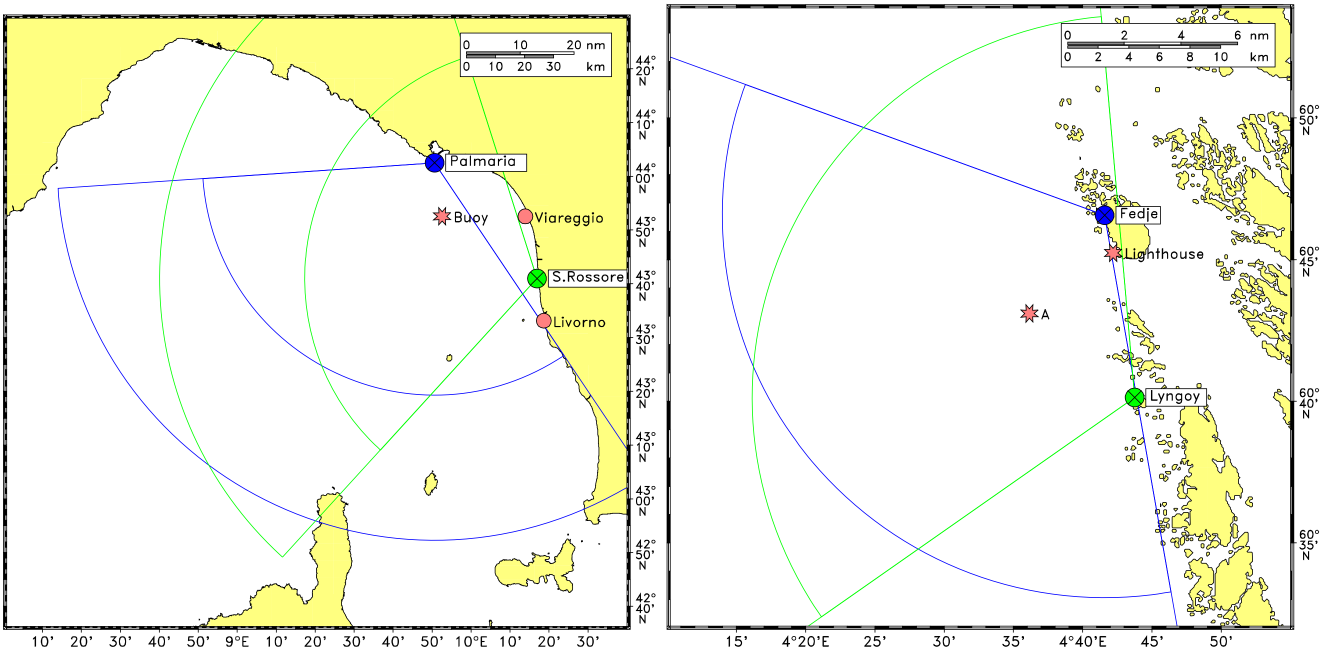

Fig. 7 *Left*, the area of the Ligurian Sea experiment showing the locations of the radars at Palmaria and San Rossore, as well as the location of the meteorological buoy. *Right*, the area of the EuroROSE Fedje experiment showing the locations of the radars at Fedje and Lyngøy islands. Wind data were collected at the light house 3 km south of the Fedje site. Mark "A" indicates the location used to verify the methods presented in this paper

In both experiments, WERA systems (cf. Gurgel et al. 1999a) were used in beam forming mode that enable accurate derivation of the second-order sidebands at a wide range of angles (±60°) allowing wave and wind inversion from second-order sidebands. Each site consisted of linear arrays of 16 receive antennas. The operating frequencies used were 12.5 and 27.68 MHz for the Ligurian Sea and Fedje experiments, respectively, corresponding to Bragg resonant ocean wavelengths of 12.0 and 5.4 m.

During the Ligurian Sea experiment the two radars were operated simultaneously collecting 9 min of data every 20 min. Wind data at a 10 min interval were obtained from a meteorological buoy deployed between the two radar sites and approximately 30 km offshore (see Fig. 7, left).

During the Fedje experiment, radar data collection rates were similar to that of the Ligurian Sea experiment. To avoid interference with each other, no simultaneous transmission was allowed and site 2 was transmitting after site 1 finished its 9 min transmission period. No in situ wind measurements were available within the radar coverage area. The nearest wind data (hourly wind speed and direction) were collected with an anemometer installed on a lighthouse, 3 km south of the Fedje radar site. In this work we assume that these wind data also apply in the vicinity of the location marked “A” in Fig. 7 (right), where our inversion methods are tested.

A histogram of the wind speeds for each experiment is shown in Fig. 8. The range of wind speeds encountered during the Norwegian Sea experiment extended up to 20 m/s; significantly higher than those measured during the Ligurian Sea where the maximum wind speeds recorded were 10 m/s. Overall 67.4% of the wind records in the Norwegian Sea exceed the 5 m/s value while only 18.9% of the total data winds exceeded that value in Italy.

5 Results

5.1 Wind-speed inversion using the first-order peak method

In this section application of the wind inversion technique described in Section 3.4.1 that uses the first-order peak method is evaluated for the two experiments.

5.1.1 Ligurian Sea experiment

During the Ligurian Sea experiment, the availability of in situ wind data enables us to test the wind inversion technique described in Section 3.4.1 that uses the power ratio of the first-order peaks from the two radar sites. The results from the ANN training, verification and testing stages are shown in Fig. 9 as scatter plots. The correlation coefficient during all ANN stages is approximately 0.7 while the root-mean-square error values range from 1.20 to 1.36 m/s. It is noticeable that most of the data points are clustered at the low wind speed region due to prevailing conditions during the experiment (see Fig. 8b). Therefore no saturation of Bragg waves appears to occur at high wind speeds, although the data in this region scatter below the 1:1 line. At low wind speeds (< 5 m/s) the ANN values fail to agree with the in situ data. However, this is not surprising as according to the theory (cf. Hasselmann et al. 1980), for this radar frequency (12.5 MHz), a minimum wind speed of 4 m/s is required for the development of ocean waves at the corresponding Bragg frequency. Under such low wind conditions, the signal registered by the radar is due to

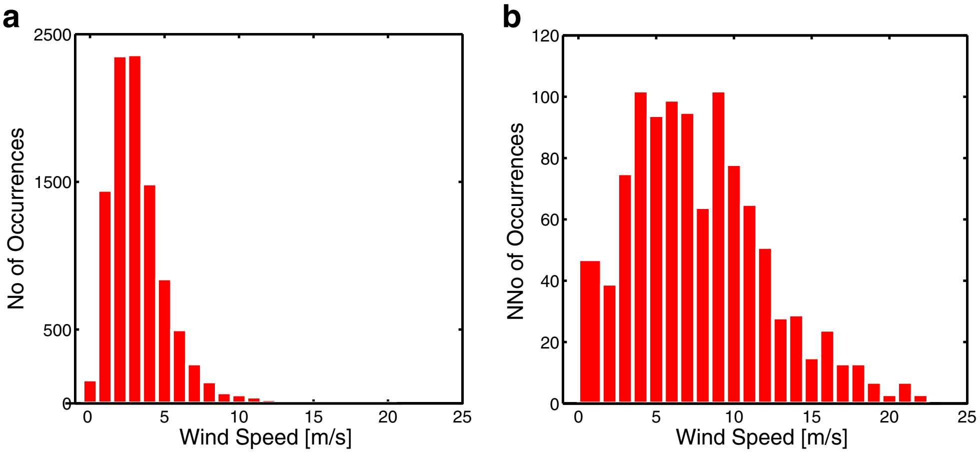

Fig. 8 Histograms of wind speed recorded during the experiments **a** at the Ligurian Sea and **b** at Fedje (Norwegian Sea)

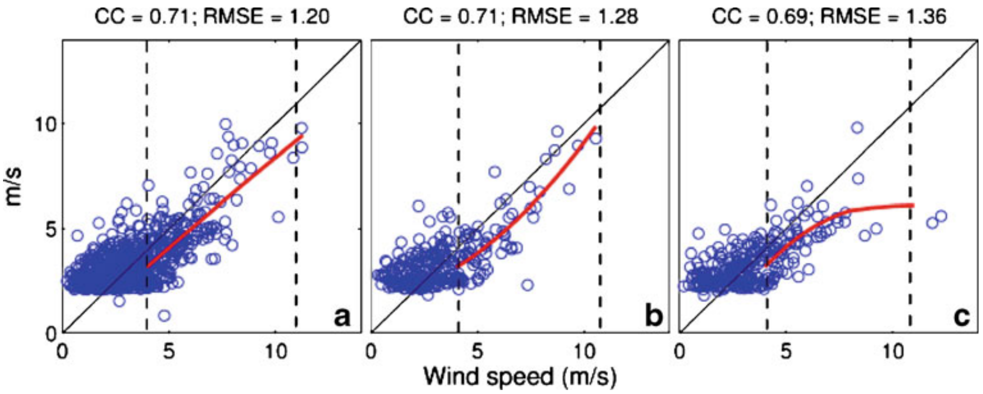

Fig. 9 Neural network performance for the first-order peak method. Scatter plot of **a** training, **b** validation, and **c** test wind speed data sets from the ANN against the in situ wind data during the Ligurian Sea experiment. The 1:1 line is shown in *black* while the *red line* is a second-order polynomial least-square-fit used to visually identify the trend of the data. Note: Correlation coefficients (*CC*) and root mean square errors (*RMSE*) are also shown. *Vertical dashed lines* define the wind speed range where Bragg waves for this radar frequency are directly related to wind speed (see text for details)

waves not associated with the prevailing atmospheric forcing and measured and inverted wind directions are not expected to match. This is in agreement with our wind speed/Bragg wave frequency analysis using the WAM-derived data set (see Section 3.1).

5.1.2 Fedje experiment

Similar analysis to the one described above was carried out for the Fedje experiment. Contrary to the Ligurian Sea experiment, this data set encompasses a wide range of wind speeds up to approximately 20 m/s (see Fig. 8a). Also, the frequency of the systems used was 27.68 MHz that corresponds to a Bragg ocean wave with wavelength and frequency of approximately 5.4 m and 0.54 Hz, respectively. At this ocean wave frequency a minimum wind speed of 2.5 m/s (lower limit) is required for the generation of wind driven waves, while the model derived wave analysis (see Section 3.1) suggested that at wind speeds greater than approximately 9 m/s (upper limit), the wave energy at this Bragg frequency saturates. The results from the different ANN development stages are shown in Figs. 10 a, b and c as scatter plots, with the lower and upper limits drawn as vertical dashed lines. The correlation coefficient during all ANN stages is on average 0.82 while the root-mean-square error values are approximately 2.1 m/s. The data scatter around the 1:1 line. However, the least-squares-fit analysis suggests a better agreement in the range of 2.5 to 9 m/s wind speed, while at higher speeds a deviation occurs in accordance with the expected saturation of wave energy. Beyond this saturation limit, methods based on second-order sidebands (e.g., Dexter and Theodorides 1982; Green et al. 2009) can be used if the signal-to-noise ratio allows.

Figure 10d–f shows the ANN wind direction results for the same data set discussed above. The direction plotted on the y-axis is calculated from the $cos\theta_W$ and $sin\theta_W$ output data of the ANN. The root-mean-square error values for the training, test and validation data are around 20°. However, some individual inversion results show large errors, possibly associated with high wind speeds. This method requires that the ANN is trained with the four peak Bragg power values only and there is not any explicit wave distribution model involved. Under low and moderate wind conditions the ANN training is sufficient to take care of any angular distribution by itself. However during storm events the Bragg peak power reaches saturation and the ANN can no longer distinguish the different situations, which may be the reason for the outliers.

5.2 Wind-speed inversion using the directional distribution of Bragg waves

In this section application of the wind inversion technique described in Section 3.4.2 that uses the directional distribution of Bragg waves method is evaluated for the two experiments.

5.2.1 Ligurian Sea experiment

The results from the ANN training, verification, and testing stages for the Ligurian Sea experiment are shown in Fig. 11 as scatter plots. The overall pattern is similar to that found for the same experiment using the

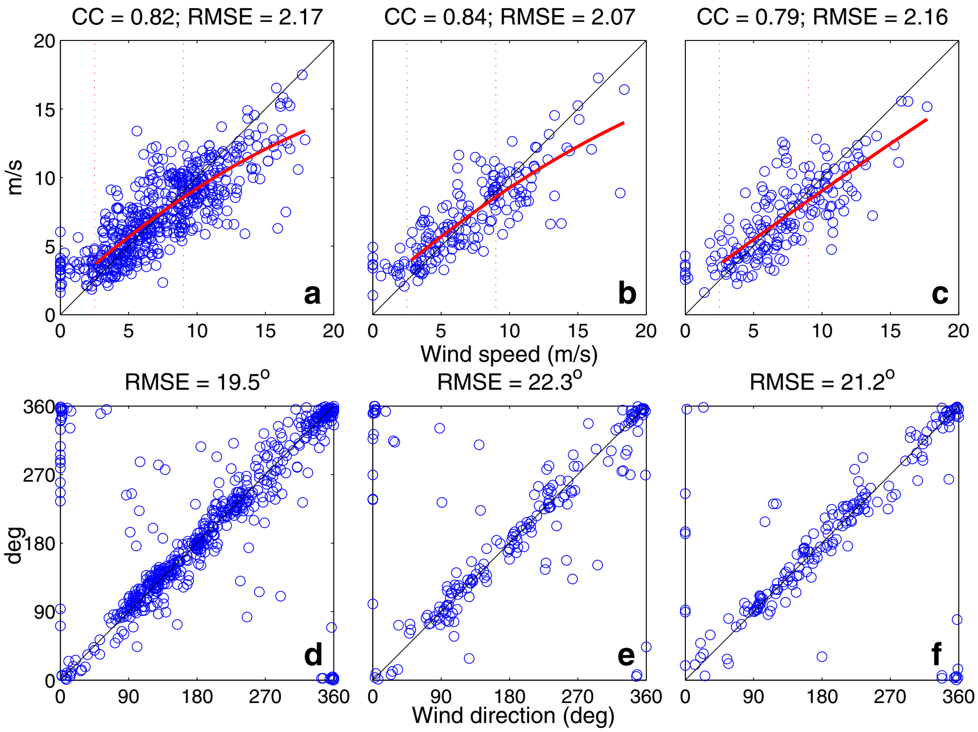

Fig. 10 Results from the Fedje experiment: **a**–**c** same as in Fig. 9. Also, scatter plots of wind direction data sets for **d** training, **e** validation, and **f** test from the ANN against wind direction measured at the lighthouse. The 1:1 line is shown in *black* and the root mean square errors (*RMSE*) are also given

first-order peak method but with significantly greater scatter around the 1:1 line indicating reduced performance. The influence of the lower limit is also visible in this example. As discussed in Section 5.1.1, measured and inverted wind directions are not expected to match.

Despite the limitations of this inversion technique, since it does not depend on radar range and beam direction, it has the advantage that it can be extended to locations different from that used for ANN training. This is shown in Fig. 12 for May 14th, 2009 at 03:00 hours. At that time, the recorded wind speed was 4.9 m/s with a direction of 128° N. The inversion technique predicted a wind speed of 5.1 m/s with a direction of 127° N. Note that in this example, the wind speed is above the lower limit required for application of the inversion technique.

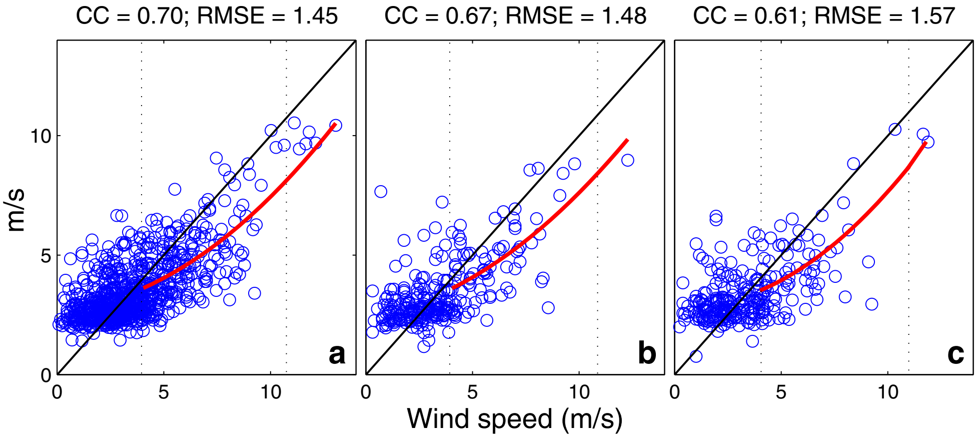

Fig. 11 Neural network performance for the directional distribution of Bragg waves method. Scatter plot of **a** training, **b** validation, and **c** test wind speed data sets from the ANN against the in situ wind data during the Ligurian Sea experiment. The 1:1 line is shown in *black* while the *red line* is a second-order polynomial least square fit used to visually identify the trend of the data. Note: Correlation coefficients (*CC*) and root mean square errors (*RMSE*) are also shown. *Vertical dashed lines* define the wind speed range where Bragg waves for this radar frequency are directly related to wind speed (see text for details)

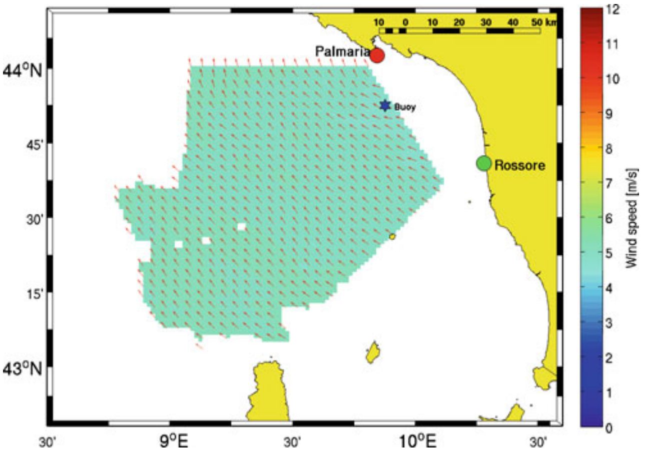

Fig. 12 Ligurian Sea experiment: wind vectors at 05/14/2009, 03:00 UTC over the whole radar coverage area derived using the directional distribution of Bragg waves method. The *arrows* indicate the direction; the color in the background gives the absolute value. The wind speed measured at the meteorological buoy at this time is 4.9 m/s from 128°

5.2.2 Fedje experiment

The wind speed results of ANN training, verification and testing stages for this experiment are shown in Fig. 13a, b and c, respectively. The upper limit saturation in this example is much clearer than it was for the first-order peak method. This difference between the two methods suggests that spreading is a much more sensitive parameter to saturation of Bragg waves while the first-order peak method partially compensates for that during the network training process.

The ANN wind direction results are shown in Fig. 13d, e and f with the direction obtained from the ANN plotted along the y-axis. The root-mean-square error values for the training, test and validation data are around 23°, which is slightly higher than that found using the first-order peak method. Again, some individual inversion results show large errors, which may be related to high wind speed causing saturation of Bragg waves and in this way introducing errors to the calculation of directional spreading.

For the relatively short Bragg waves and high wind speeds encountered during this experiment both Bragg wave and wind directions are expected to be almost identical so that the ANN predicted direction should not be significantly different. A comparison of the measured Bragg wave and ANN predicted directions (not shown here) revealed a root-mean-square difference of approximately 15°.

Similar to the Ligurian Sea experiment, the method allows us to extend wind vector estimates over the whole radar coverage area, as shown in Fig. 14 for March 31st, 2000 at 15:00 hours.

The recorded wind speed at location “A”–see star symbol in Fig. 7, right—was 7.2 m/s with a direction

Fig. 13 Results from the Fedje experiment: **a**–**c** same as in Fig. 11. Also, scatter plots of wind direction data sets for **d** training, **e** validation, and **f** test from the ANN against wind direction measured at the lighthouse. The 1:1 line is shown in *black* and the root mean square errors (*RMSE*) are also given

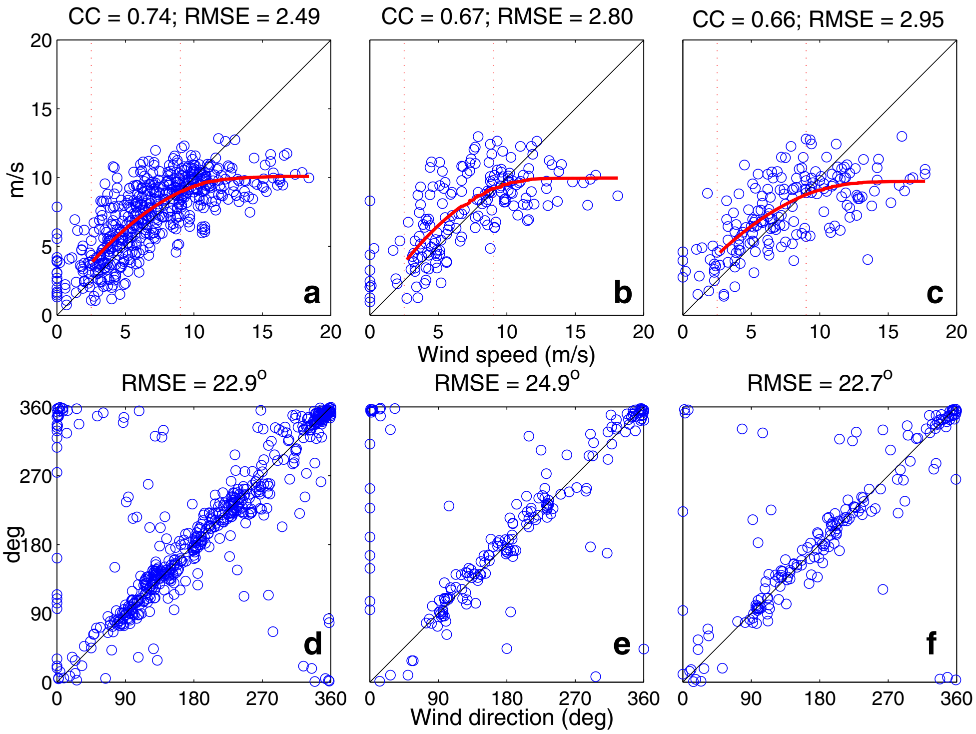

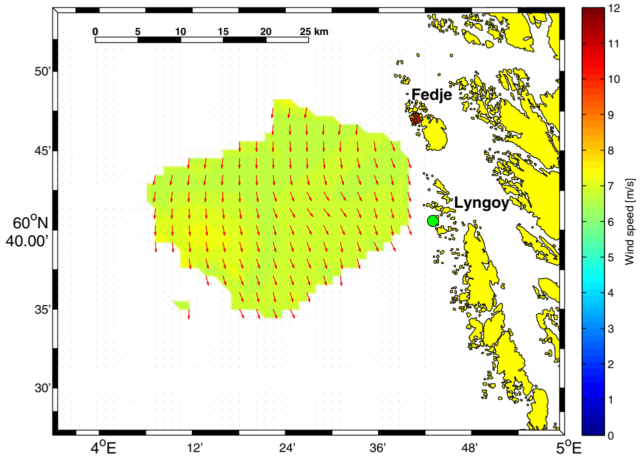

Fig. 14 Fedje experiment: wind vectors at 03/31/2000, 15:00 UTC over the whole radar coverage area derived using the directional distribution of Bragg waves method. The *arrows* indicate the direction; the color in the background gives the absolute value. The wind speed measured at the meteorological buoy at this time is 7.2 m/s from 340°

of 340° N, while the inverted speed is 7.1 m/s with a direction of 347° N. Spatial variability both in speed and direction can be seen in the figure, although we can not verify its accuracy. Figure 14 shows a typical result for a situation when the first-order Bragg peak power was not saturated.

5.3 Method limitations

The comparison between wind inversion techniques and actual data showed a significant scatter with increased scatter for the method that includes the azimuthal distribution of the waves. The latter might indicate problems with the selection of the directional distribution model used. In addition, this scatter can be attributed to measurement errors and/or natural spatial and temporal variability of the area of the ocean the radar signal is scattered from.

The in situ wind data for the experiments presented in here and the radar signal represent temporal averages over similar time periods (10 and 9 min for the wind and radar data, respectively). This suggests that no differences due to the integration time are expected. However, given that the radar sees wind waves, this suggestion assumes a linear relationship between wind and waves, which is not the case. Within the averaging time period (10 min in this study) a mean wind speed value is estimated, there are a number of short term wind variations (gusts and squalls) that have significantly lower temporal (1 to 2 min) variations. This is well known in meteorology and a gust factor has been developed which is defined as the peak over mean wind speed. This factor is used to relate mean wind speed to the maximum wind occurring during the time interval utilized to estimate the mean value (cf. Tattelman 1975). It was found that the gust factor decreases with increasing wind speed, suggesting more gusts being present at lower wind speeds. Lavrenov (2003) characterizes these wind oscillations and he used a numerical simulation to evaluate their effect in the development of wind wave spectrum. The wind gust effects were parameterized as quasi-oscillations and were numerically approximated as fluctuations of the JONSWAP spectrum (cf. Hasselman et al. 1973). The results showed that such oscillations in wind produce a significant effect on the non-linear wave spectrum evolution. This effect was more significant at the initial stages of development of a wind spectrum and becomes smaller for a developed sea suggesting more effects under low wind conditions.

Introduction of this variability in the first-order cross-section equation (Eq. 4) could lead to variability of the first-order Bragg ratio. At present, the non-linear nature of such variability makes it difficult to account for and more theoretical work is required. In order to obtain some additional information on the impact of this variability on the power of the first-order Bragg peaks, 55 min of coherent backscatter signals measured at the Palmaria site (12.5 MHz) have been investigated. 99 spectra with 512 samples each, 2.22 min integration time and 75% overlap in time have been calculated. A time stack of these spectra is shown in Fig. 15a. Figure 15b gives the power of the Bragg peaks for each individual spectrum (2.22 min) and averaging five and ten spectra (4.44 min and 7.21 min, respectively). Figure 15c shows the power ratio of the Bragg peaks, which is used to find the direction of the Bragg waves with respect to the radar look direction. Note that a strong variability is observed for the single spectra. This variability is reduced when averaging five spectra and it almost disappears when averaging ten spectra. The angle between the radar look direction and the wind direction measured by the meteorological buoy is shown in Fig. 15d. Note that the changes in wind direction measured at the buoy and the Bragg peak ratio for 7.21 min averages are closely related to each other. As the integration time of the HF radar data was set to 9 min, the impact of the first-order Bragg peak variability on the results of the ANN methods is considered to be insignificant.

As discussed earlier, the clutter observed in the results from the ANN methods can be caused by the directional model selected for fitting the Bragg peak

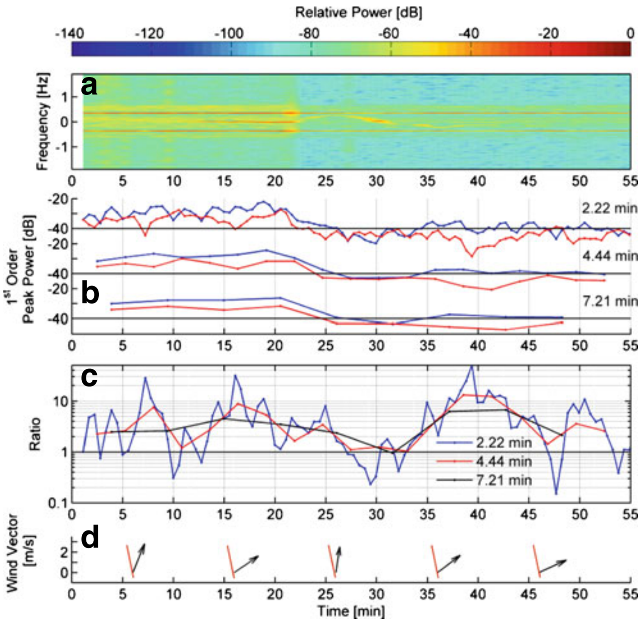

Fig. 15 Doppler spectra and first-order peak power variability over a period of 55 min from the 12.5 MHz radar at Palmaria during the Ligurian Sea experiment for a range cell and beam direction coinciding with the location of the meteorological buoy (see Fig. 7). **a** Time stack of individual Doppler spectra estimated using 512 points with a 75% overlap. **b** First-order peak power levels for positive (*blue*) and negative (*red*) Bragg frequencies. Estimates from individual spectra (2.22 min) and averaged spectra of five and ten segments (4.44 min and 7.21 min, respectively) are shown. **c** Ratio of positive over negative frequency first-order peak power of the estimates shown in **b**. **d** Ten min averaged wind vectors from the meteorological buoy (*red line* indicates radar beam direction at the buoy location)

ratio. The model used here is the $\mathrm{sech}^2(\beta \cdot \theta)$ distribution (see Eq. 1), which was identified to give the most realistic up/down wind ratio compared with measurements (cf. Gurgel et al. 2006). In case of a different directional model such as a cardioid model with a wind speed dependent exponent (e.g. Tyler et al. 1974) or other directional models such as those described in Elfouhaily et al. (1997) or Kudryavtsev et al. (2005) the expectation is that the ANN will train itself to identify the differences through the training process. A more significant problem might arise in cases of bimodal wave directionality. Gagnaire et al. (2010) (see their Fig. 12) showed that for frequencies twice the peak frequency the directionality of the spectrum becomes bimodal with the majority of the energy being focused at ±60 degrees from the wind mean direction. Such bimodality is not represented in the model used in this study. Unfortunately the buoy measured directional information available for the Fedje experiment are based on a cosine-2s directional model and as such are constrained by the model used. We do not have directional model independent information on the wave spectrum to prove if our selection of the directional model introduces problems in the inversion, although the ability of the ANN to train itself under such conditions is unclear.

6 Conclusions

Two new methods for the extraction of wind speed estimates using the first-order peak energy of HF radar backscatter Doppler spectra have been presented. Both methods utilize ANNs to fit the non-linear relationship between wind and Bragg ocean waves and require data from at least two radar sites. One of the methods is based on the first-order peaks while the other one uses the spreading of the directional distribution of Bragg waves. The latter method, although less accurate than the former, can be extended throughout the radar coverage area. Both methods require wind speeds greater than the phase velocity of the ocean wave at the Bragg frequency (low limit condition). At high wind speeds, wave energy saturation limits applicability of the methods with the first-order peak method being less sensitive to this effect.

For wind-speed inversion from HF radar first-order peaks, the new methods can be applied at low and moderate wind speeds (greater than the lower limit for the particular frequency used) while application of existing second-order methods will be limited to shorter ranges due to the reduced signal-to-noise ratios. Above the saturation limit the methods based on analysis of the second-order signal are more suitable as its signal-to-noise ratio increases with higher wind speeds. A hybrid of first- and second-order methods is recommended for operational use.

Regarding the portability of the trained ANNs to other locations or radar frequencies, there are some limitations to be taken into account. The application of ANN as presented in this work is valid only for the environmental conditions (winds and wind-generated waves) and radar frequencies used during the training and validation of the network. The ANN will not be transferable to different HF radar frequency systems even if they operate on the same site, as these new systems will be extracting information from a different part of the spectrum not used in the training of the network. Application of the ANN with a system of the same frequency but on a different location could be used with caution as there are variables (e.g., fetch) that could change the f_B/f_p ratio and, thus, the part of the spectrum seen by the radar. Depending on how much this ratio changes it could potentially invalidate the ANN training. Despite these limitations, the strength of the method lies in the fact that training of the ANN can be achieved through the deployment of an in situ station for a limited period of time and once the training has been completed then the ANN supported inversion can be used for long-term HF radar operation.

This effort has presented the fundamentals for using the first-order Bragg resonant scatter signal for estimating wind data using HF radars, and it presented some methods and preliminary results. However, more work is required for its validation under different wind conditions and for different directional distributions.

Acknowledgments The authors would like to thank Heinz Günther from the Helmholz–Zentrum Geesthacht (former GKSS Research Center) for providing the HIPOCAS WAM model data, the EuroROSE consortium for providing the Fedje experiment data set, and NURC for providing the Ligurian Sea experiment data set to Klaus-Werner Gurgel. The first author was supported by the China Scholarship Council while Deutscher Akademischer Austausch Dienst (DAAD) provided a research grant to George Voulgaris for his visit to the University of Hamburg. Finally, the authors would like to acknowledge the contribution of the two anonymous reviewers whose comments helped us improve this manuscript.

References

Apel J (1994) An improved model of the ocean surface wave vector spectrum and its effects on radar backscatter. J Geophys Res 99(C8):16269–16291. doi:10.1029/94JC00846

Banner M (1990) Equilibrium spectra of wind waves. J Phys Oceanogr 20:966–985

Banner M, Jones I, Trinder J (1989) Wavenumber spectra of short gravity waves. J Fluid Mech 198:321–344. doi:10.1017/S0022112089000157

Barrick D (1971a) Theory of HF and VHF propagation across the Rough Sea, part I: the effective surface impedance for a slightly rough highly conducting medium at grazing incidence. Radio Sci 6(5):517–526. doi:10.1029/RS006i005p00517

Barrick D (1971b) Theory of HF and VHF propagation across the Rough Sea, part II: application to HF and VHF propagation above the sea. Radio Sci 6(5):527–533. doi:10.1029/RS006i005p00527

Barrick D (1972a) First-order theory and analysis of MF/HF/VHF surface from the sea. IEEE Trans Antennas Propag 20:2–10

Barrick D (1972b) Remote sensing of sea state by radar. In: Derr VE (ed) Remote sensing of the troposphere. US Government Printing Office, Washington

Barrick D (1977a) Extraction of wave parameters from measured HF radar sea-echo Doppler spectra. Radio Sci 12(3):415–424

Barrick D (1977b) Ocean surface current mapped by radar. Science 198:138–144

Barrick D (1977c) The ocean waveheight nondirectional spectrum from inversion of the HF sea-echo Doppler spectrum. Remote Sens Environ 6:201–227. doi:10.1016/0034-4257(77)90004-9

Barrick D, Headrick J, Bogle R, Crombie D (1974) Sea backscatter at HF: interpretation and utilization of the echo. In: Proc. IEEE, vol 62(6)

Crombie D (1955) Doppler spectrum of sea echo at 13.56 Mc./s. Nature 4459:681–682. doi:10.1038/175681a0

Demuth H, Beale M, Hagan M (2009) Neural network toolbox 6—user's guide. Mathworks Inc, Natick

Dexter P, Theodorides S (1982) Surface wind speed extraction from HF sky-wave radar Doppler spectra. Radio Sci 17(3):643–652

Donelan M, Pierson W Jr (1987) Radar scattering and equilibrium ranges in wind-generated waves with application to scatterometry. J Geophys Res 92(C5):4971–5029. doi:10.1029/JC092iC05p04971

Donelan M, Hamilton J, Hui W (1985) Directional spectra of wind-generated waves. Philos Trans R Soc Lond Ser A Math Phys Sci 315:509–562

Elfouhaily T, Chapron B, Katsaros K, Vandemark D (1997) A unified directional spectrum for long and short wind-driven waves. J Geophys Res 102(C7):15,781–15,796. doi:10.1029/97JC00467

Fisher C, Young G, Winstead N, Haqq-Misra J (2008) Comparison of synthetic aperture radar-derived wind speeds with buoy wind speeds along the mountainous Alaskan Coast. J Appl Meterol Climatol 47:1365–1376. doi:10.1175/2007JAMC1716.1

Forget P, Broche P, de Maistre J (1982) Attenuation with distance and wind speed of HF surface waves over the ocean. Radio Sci 17(3):599–610. doi:10.1029/RS017i003p00599

Gagnaire E, Benoit M, Forget P (2010) Ocean wave spectrum properties as derived from quasi-exact computations of nonlinear wave-wave interactions. J Geophys Res 115(C12058):1–24. doi:10.1029/2009JC005665

Gill E, Walsh J (2001) High-frequency bistatic cross sections of ocean surface. Radio Sci 36(6):1459–1475

Green D, Gill E, Huang W (2009) An inversion method for extraction of wind speed from high-frequency ground-wave radar oceanic backscatter. IEEE Trans Geosci Remote Sens 47(10):3338–3346

Günther H, Gurgel KW, Evensen G, Wyatt L, Guddal J, Borge JN, Reichert K, Rosenthal W (1998) EuroROSE—European radar ocean sensing. In: Proceedings of the COST conference provision and engineering/operational application of wave spectra. Paris, France, 21–25 September 1998

Gurgel KW, Antonischki G, Essen HH, Schlick T (1999a) Wellen radar (WERA): a new ground-wave HF radar for ocean remote sensing. Coast Eng 37:219–234

Gurgel KW, Essen HH, Kingsley S (1999b) HF radars: physical limitation and recent developments. Coast Eng 37:201–218

Gurgel KW, Essen HH, Schlick T (2006) An empirical method to derive ocean waves from second-order Bragg scattering: prospects and limitations. IEEE J Oceanic Eng 31(4):804–811

Gurgel KW, Schlick T, Voulgaris G, Seemann J, Ziemer F (2011) HF radar observations in the German bight: measurements and quality control. In: Proceedings of the tenth IEEE/OES current, waves and turbulence measurement workshop (CWTM), Monterey, California, USA, 20–23 March 2011

Harlan J, Georges T (1994) An empirical relation between ocean-surface wind direction and the Bragg line ratio of HF radar sea echo spectra. J Geophys Res 99(C4):7971–7978

Hasselman K, Barnett T, Bouws E, Carlson H, Cartwright D, Enke K, Ewing J, Gienapp H, Hasselmann D, Kruseman P, Meerburg A, Müller P, Olbers D, Richter K, Sell W, Walden H (1973) Measurements of wind-wave growth and swell decay during the joint north sea wave project (JONSWAP). Ergänzungsheft zur Deutschen Hydrographischen Zeitschrift 8(12):95

Hasselmann K (1971) Determination of ocean wave spectra from Doppler radio return from the sea surface. Nat Phys Sci 229:16–17. doi:10.1038/physci229016a0

Hasselmann D, Dunckel M, Ewing J (1980) Directional wave spectra observed during JONSWAP 1973. J Phys Oceanogr 10:1264–1280

Hasselmann S, Hasselmann K, Bauer E, Janssen P, Komen G, Bertotti L, Lionello P, Guillaume A, Cardone V, Greenwood J, Reistad M, Zambresky L, Ewing J (1988) The WAM model—a third generation ocean waves prediction model. J Phys Oceanogr 18:1775–1810

Haus B, Work P, Voulgaris G, Shay N, Ramos R, Martinez J (2010) Wind speed dependence of single site wave height retrievals from phased-array HF radars. J Geophys Res 27:1381–1394. doi:10.1175/2010JTECHO730.1

Heron M, Rose R (1986) On the application of HF ocean radar to the observation of temporal and spatial changes in wind direction. IEEE J Oceanic Eng OE-11(2):210–218

Heron M, Prytz A (2002) Wave height and wind direction from the HF coastal ocean surface radar. Can J Remote Sens 28(3):385–393

Kaastra I, Boyd M (1996) Designing a neural network for forecasting financial and economic time series. Neurocomputing 10:215–236

Kudryavtsev V, Akimov D, Johannessen J, Chapron B (2005) On radar imaging of current features: 1. Model and comparison with observations. J Geophys Res 110(C07016):1–27. doi:10.1029/2004JC002505

Lavrenov I (2003) Wind-waves in oceans: dynamics and numerial simulations. Springer, Berlin

Marquardt D (1963) An algorithm for least-squares estimation of nonlinear parameters. J Soc Ind Appl Math 11(2):431–441

Monaldo F, Thompson D, Beal R, Pichel W, Clemente-Colon P (2001) Comparison of SAR-derived wind speed with model predictions and ocean buoy measurements. IEEE Trans Geosci Remote Sens 39(12):2587–2600. doi:10.1109/36.974994

Parks A, Shay L, Johns W, Martinez-Pedraja J, Gurgel KW (2009) HF radar observations of small-scale surface current variability in the straits of Florida. J Geophys Res 114:C08,002, 1–17. doi:10.1029/2008JC005025

Pierson W, Moskowitz L (1964) A proposed spectral form of fully developed wind seas based on similarity theory of S.A. Kitaigorodskii. J Geophys Res C,69:5191–5204

Rojas R (1996) Neural networks: a systematic introduction. Springer, Berlin

Rumelhart D, Hinton G, Williams R (1986) Learning representations by back-propagating errors. Nature 323:533–536. doi:10.1038/323533a0/

Savidge D, Amft J, Gargett A, Archer M, Conley D, Voulgaris G, Wyatt L, Gurgel KW (2011) Assessment of WERA long-range HF-radar performance from the user's perspective. In: Proceedings of the tenth IEEE/OES current, waves and turbulence measurement workshop (CWTM). Monterey, California, USA, 20–23 March 2011

Schroeder L, Schaffner P, Mitchell J, Jones W (1985) AAFE RADSCAT 13.9-GHz measurements and analysis: wind-speed signature of the ocean. IEEE J Oceanic Eng 10(4):346–357. doi:10.1109/JOE.1985.1145123

Shearman E (1983) Propagation and scattering in mf/hf groundwave radar. In: IEE Proceedings F, vol 130(7), pp 579–590. doi:10.1049/ip-f-1:19830092

Soares CG (2008) Hindcast of dynamic processes of the ocean and coastal areas of Europe. Coast Eng 55(11):825–826. doi:10.1016/j.coastaleng.2008.02.007

Stewart, RH and Barnum, JR (1975) Radio measurements of oceanic winds at long ranges: an evaluation. Radio Sci 10(10):853–857. doi:10.1029/RS010i010p00853

Tattelman P (1975) Surface gustiness and wind speed range as a function of time interval and mean wind speed. J Appl Meteorol 14(7):1271–1276

Tyler G, Teague C, Stewart R, Peterson A, Munk W, Joy J (1974) Wave directional spectra from synthetic aperture observations of radio scatter. Deep Sea Res 21(12):989–1016. doi:10.1016/0011-7471(74)90063-1

Vesecky J, Drake J, Laws K, Ludwig F, Teague C, Paduan J, Meadows L (2005) Using multifrequency HF radar to estimate ocean wind fields. In: Proceedings of the 25th IEEE international geoscience and remote sensing symposium (IGARSS 2005), Seoul, Korea, 25–29 July 2005

Wyatt L (1986) The measurement of the ocean wave directional spectrum from HF radar Doppler spectra. Radio Sci 21(3):473–485

Wyatt L, Green J, Middleditch A, Moorhead M, Howarth J, Holt M, Keogh S (2006) Operational wave, current, and wind measurements with the pisces HF radar. IEEE J Oceanic Eng 31(4):819–834. doi:10.1109/JOE.2006.888378